

Transmission electron microscopy characterization of colloidal copper nanoparticles and their chemical reactivity

Guangjun Cheng · A. R. Hight Walker

Received: 6 August 2009 / Revised: 25 September 2009 / Accepted: 28 September 2009 / Published online: 16 October 2009
© US Government 2009

Abstract A colloidal synthesis method was developed to produce face centered cubic (fcc) Cu nanoparticles in the presence of surfactants in an organic solvent under an Ar environment. Various synthetic conditions were explored to control the size of the as-prepared nanoparticles by changing the precursor, varying the amount of surfactants, and tuning the reaction temperature. Transmission electron microscopy (TEM), selected-area electron diffraction, and high-resolution TEM were used as the main characterization tools. Upon exposure to air, these nanoparticles are oxidized at different levels depending on their sizes: (1) an inhomogeneous layer of fcc Cu₂O forms at the surface of Cu nanoparticles (about 30 nm); (2) Cu nanoparticles (about 5 nm) are immediately oxidized into fcc Cu₂O nanoparticles (about 6 nm). The occurrence of these different levels of oxidization demonstrates the reactive nature of Cu nanoparticles and the effect of size on their reactivity. Furthermore, utilization of their chemical reactivity and conversion of spherical Cu nanoparticles into CuS nanoplates through the nanoscale Kirkendall effect were demonstrated. The oxidization and sulfidation of Cu nanoparticles were compared. Different diffusion and growth behaviors were involved in these two chemical transformations, resulting in the formation

of isotropic Cu₂O nanoparticles during oxidization and anisotropic CuS nanoplates during sulfidation.

Keywords Copper nanoparticles · Copper oxide nanoparticles · Copper sulfide nanoplates · Kirkendall effect · Nanoplates · Transmission electron microscopy

Introduction

Chemically synthesized nanoparticles with controllable size and shape have recently been used as templates to create more complex nanoparticles, which has greatly expanded the applications of nanoparticles in the fields of electronics, optics, energy, catalysis, and biology [1–3]. For example, hollow nanoparticles have been produced through the nanoscale Kirkendall effect by introducing a reactive reagent into colloids containing presynthesized solid nanoparticles and creating a nonequilibrium diffusion process between two components [4–7]. Characterizing and understanding the stability and chemical reactivity of the preengineered nanoparticles are critical for their further usage as templates to produce new nanostructures. In addition, this knowledge will help to address the increasing concerns associated with their toxicity and environmental health and safety [8, 9].

The reactivity of nanoparticles can pose challenges for their own synthesis and characterization. An example is the case of Cu nanoparticles. Similar to Au and Ag nanoparticles, Cu nanoparticles adopt a face centered cubic (fcc) structure and exhibit surface plasmon resonance in the visible region. However, owing to their high reactivity with respect to oxidization in air, there is only limited work on their synthesis and characterization, in comparison with the extensive research on Au and Ag nanoparticles [3]. Even among the limited work, there are

Disclaimer We identify certain commercial equipment, instruments, and materials in this article to specify adequately the experimental procedure. In no case does such identification imply recommendation or endorsement by the National Institute of Standards and Technology, nor does it imply that the materials or equipment identified are necessarily the best available for the purpose.

G. Cheng (✉) · A. R. Hight Walker
Optical Technology Division, Physics Laboratory,
National Institute of Standards and Technology,
Gaithersburg, MD 20899, USA
e-mail: guangjun.cheng@nist.gov

some controversial results in the literature and it has been suggested that more experiments are needed to verify whether Cu nanoparticles or copper oxide nanoparticles are actually prepared [3].

For the synthesis of Cu nanoparticles, since 1993, Peileni's group [10–13] has focused on using reverse micelles through the reduction of copper(II) bis(2-ethyl-hexyl)sulfosuccinate by hydrazine at room temperature. With the advancement in the synthesis of monodisperse and highly crystalline transition metal and transition metal oxide nanoparticles using thermal decomposition or thermal reduction in an organic solvent [1, 14], these methods have been used to synthesize Cu nanoparticles. Recently, it has been demonstrated that Cu nanoparticles can be produced through the thermal decomposition of copper(I) acetate [Cu(ac)] in the presence of surfactants at 543 K. However, these Cu nanoparticles can be easily transformed into Cu₂O [15]. The synthesis of Cu nanoparticles through the thermal reduction of copper(II) acetylacetonate [Cu(acac)₂] using 1,2-hexadecanediol (HDD) in octyl ether has been reported and Cu nanoparticles ranging from 5 to 25 nm have been synthesized by changing the reaction temperature [16].

On the basis of our previous work on the synthesis of Co [17–21] and Ni nanoparticles [22], we developed a colloidal synthesis method to synthesize Cu nanoparticles via thermal decomposition of Cu(ac) or thermal reduction of Cu(ac) or Cu(acac)₂ using HDD in benzyl ether (BE) under an Ar environment. The synthetic conditions were varied to better control the size and size distribution of the as-prepared Cu nanoparticles. We also probed their reactivity with respect to their oxidization in air. Cu nanoparticles of different size, prepared under similar synthetic conditions, were used to investigate the effect of their size on this oxidization process. Finally, we demonstrated the conversion of spherical Cu nanoparticles into CuS nanoplates through the nanoscale Kirkendall effect. Here, copper oxide and copper sulfide were chosen because of their applications in solar energy conversion and catalysis [15, 23–25]. Owing to the distinct crystalline structures of Cu, Cu₂O, and CuS, we focused on our characterization of these as-prepared Cu nanoparticles and their transformations to copper oxide and copper sulfide mainly using transmission electron microscopy (TEM), selected-area electron diffraction (SAED), and high-resolution TEM (HRTEM) since these techniques are powerful and direct in characterizing the morphology and structural transformations of nanoscale materials [26, 27]. Considering the rich variety of the copper sulfide family, such as Cu₂S, Cu_{1.97}S, Cu_{1.8}S, and Cu_{1.4}S, and each with its own structure and band gap [25], we also expect this work will open an avenue for synthesizing a variety of copper sulfides.

Experimental

Chemicals

Cu(acac)₂ (97%), Cu(ac) (97%), S (99.98%), oleic acid (OA; 99%), oleylamine (OAmine; 70%), HDD (90%), and BE (99%) were purchased from Aldrich (Milwaukee, WI, USA). All chemicals were used without further treatment.

Synthesis of Cu nanoparticles

Cu nanoparticles were synthesized under an Ar environment. Table 1 lists the synthetic conditions for the five batches of Cu nanoparticles reported here; they are labeled from A to E. Cu(acac)₂ or Cu(ac) was used as the precursor with BE as the solvent. OA and OAmine were used as the surfactants. Except for the synthesis of sample A, HDD was used as the reducing agent.

For the synthesis of sample A, Cu(ac), OA, OAmine, and BE were mixed in a flask and degassed in Ar for 20 min. The mixture was heated to 383 K and kept at this temperature for 10 min. Then the reaction temperature was raised to 523 K and the reaction was continued for 10 min.

For the synthesis of sample B, Cu(acac)₂, OA, OAmine, HDD, and BE were mixed in a flask and degassed in Ar for 20 min. The mixture was heated to 383 K and kept at this temperature for 10 min. Then the reaction temperature was raised to the reflux temperature of BE (about 570 K) and the reaction was continued for 10 min.

For the synthesis of sample C, OA, OAmine, HDD, and BE were mixed in a flask and degassed in Ar for 20 min. The mixture was heated to the reflux temperature of BE (about 570 K). Then the precursor solution [Cu(acac)₂ dissolved in BE] was quickly injected into the mixture. The reaction was continued for 5 min.

For the synthesis of samples D and E, Cu precursor, OA, OAmine, HDD, and BE were mixed in a flask and degassed in Ar for 20 min. The mixture was heated to 383 K and kept at this temperature for 10 min. Then the reaction temperature was raised to 473 K and the reaction was continued for 40 min.

At the end of the syntheses, the colloids were extracted using an airtight syringe and stored in glass vials.

Synthesis of CuS nanoplates

After about 5 mL colloid of sample D had been removed from the reaction flask at the end of the Cu nanoparticle synthesis for the characterization, the remaining colloid was used to synthesize CuS nanoplates. The solution of S (12 mg) dissolved in BE (5 mL) was quickly injected into the colloid left in the flask at 473 K under an Ar environment (the molar ratio of S to Cu approximately was 1:1). The reaction was continued for another 20 min before the mixture was cooled to

Table 1 Sample information for the five batches of Cu nanoparticles synthesized in this work

Sample	Copper precursor	Surfactants/solvent/reducing agent	Reaction conditions	Diameter (nm)
A	0.06 g Cu(ac)	0.2 mL OA + 0.2 mL OAmine/20 mL BE/no HDD	383 K/10 min 523 K/10 min	54±9
B	0.13 g Cu(acac) ₂	0.16 mL OA + 0.17 mL OAmine/20 mL BE/0.4 g HDD	383 K/10 min 570 K/10 min	76±20
C	0.13 g Cu(acac) ₂ /2 mL BE	0.16 mL OA + 0.17 mL OAmine/10 mL BE/0.4 g HDD	Quick injection 570 K/5 min	70±24
D	0.06 g Cu(ac)	0.16 mL OA + 0.17 mL OAmine/20 mL BE/0.4 g HDD	383 K/10 min 473 K/40 min	29±9
E	0.06 g Cu(ac)	1 mL OA + 2 mL OAmine/20 mL BE/0.4 g HDD	383 K/10 min 473 K/40 min	5.0±0.7

Cu(ac) copper(I) acetate, *Cu(acac)₂* copper(II) acetylacetonate, *OA* oleic acid, *OAmine* oleylamine, *BE* benzyl ether, *HDD* 1,2-hexadecanediol

room temperature. The as-prepared colloid was extracted using an airtight syringe and stored in a glass vial. The same procedure was also applied to convert the Cu nanoparticles in sample E into CuS nanoplates.

TEM characterization

TEM and HRTEM images and SAED patterns for colloidal Cu nanoparticles and their transformation to Cu₂O nanoparticles or CuS nanoplates were obtained using a JEOL 2100 LaB₆ transmission electron microscope (200 kV). TEM samples were prepared by dropping the colloids onto carbon-coated TEM grids (Formvar/carbon Cu grids, Ted Pella, Redding, CA, USA) and allowing the liquid carrier to evaporate in air.

Results

Cu nanoparticles in samples A, B, and C

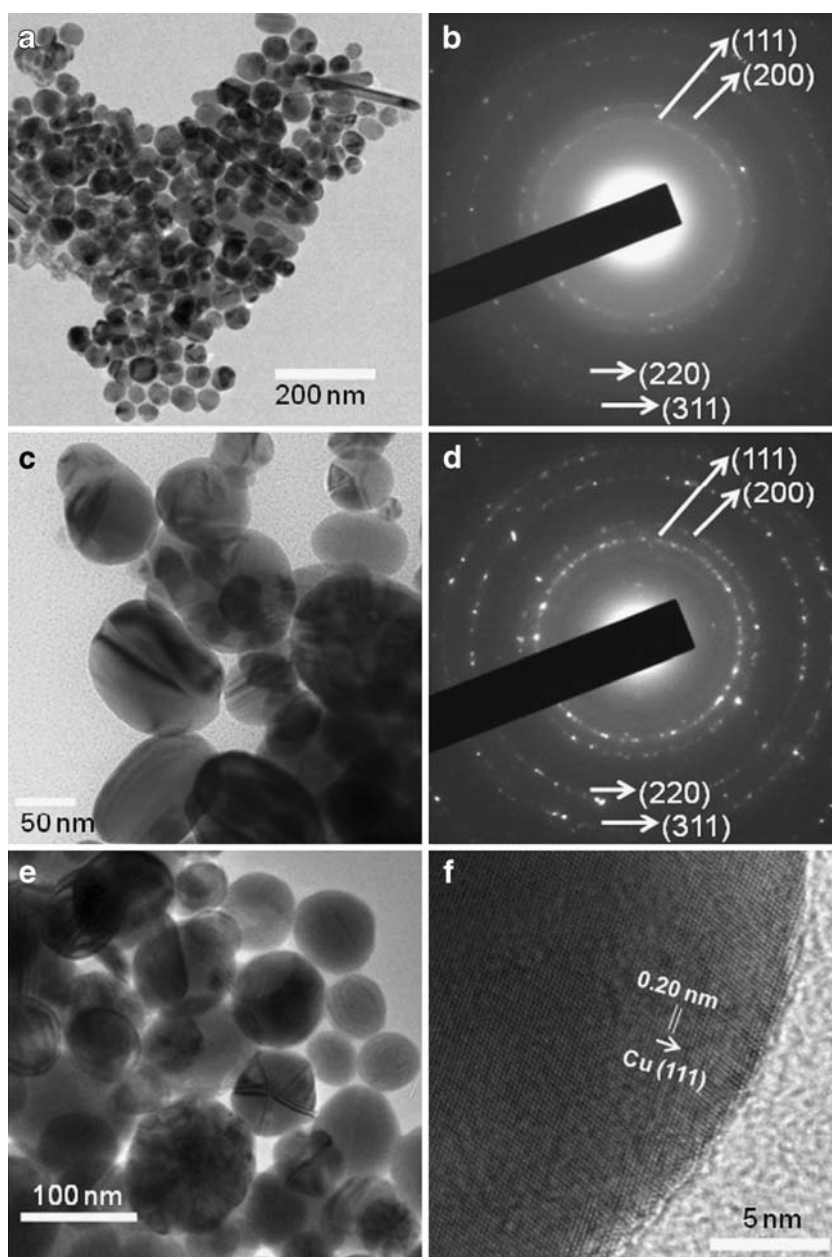
In our previous work, we successfully synthesized monodisperse and highly crystalline Co and Ni nanoparticles in an organic solvent by thermal decomposition of dicobalt octacarbonyl [17–21] and bis(1,5-cyclooctadiene)nickel [22], respectively. To extend this method to Cu nanoparticles, Cu(ac), with a decomposition temperature of 523 K, was selected as the precursor owing to its commercial availability. BE has a high boiling point (about 570 K) and provides a large temperature window for the reaction. As the mixture of Cu(ac), OA, OAmine, and BE was heated to 383 K from room temperature in the synthesis of sample A, the color of the solution changed from green to dark blue. As the reaction temperature rose to 523 K, the solution went through a series of color changes from dark blue, green, yellow, dark brown to burgundy. After 10 min at 523 K, a dark-red colloid was collected. Figure 1a shows a typical TEM image of the as-prepared Cu nanoparticles in sample A. Most of the as-prepared

nanoparticles are spherical. The average diameter of these spherical Cu nanoparticles was determined to be 54 nm with a standard deviation of 9 nm. A few Cu nanorods ranging from 100 to 400 nm in length were also obtained. Most of the nanoparticles show inhomogeneous contrast regions within one nanoparticle, indicating their polycrystalline structure. Figure 1b shows the SAED pattern of the as-prepared Cu nanoparticles in sample A. Four distinct diffraction rings are observed and their corresponding interplanar spacing values were calculated to be 0.2, 0.18, 0.13, and 0.11 nm. These values are in agreement with the ones for fcc Cu (JCPDF no. 71-4610, *Fm-3m*, $a=0.3617$ nm, $d_{111}=0.20883$ nm, $d_{200}=0.18085$ nm, $d_{220}=0.12788$ nm, and $d_{311}=0.10906$ nm). Therefore, the rings in Fig. 1b are indexed as their corresponding fcc Cu crystalline planes.

Our previous work demonstrated that utilizing the high boiling point of an organic solvent and performing thermal decomposition at its boiling point are critical for the growth of Ni nanoparticles [22]. Since thermal reduction is also an effective way to prepare monodisperse and highly crystalline metallic nanoparticles, in the synthesis of sample B, thermal reduction of Cu(acac)₂ using HDD as the reducing agent was performed at the boiling point of BE. After 10 min at 570 K, a dark-red colloid was collected. Figure 1c shows a typical TEM image of the as-prepared Cu nanoparticles in sample B. The average diameter was determined to be 76 nm with a standard deviation of 20 nm. The SAED pattern of the as-prepared Cu nanoparticles in sample B shown in Fig. 1d exhibits four diffraction rings similar to those shown in Fig. 1b and these rings are indexed as their corresponding fcc Cu crystalline planes.

A rapid thermal reduction of Cu(acac)₂ was performed in the synthesis of sample C. When the Cu precursor solution [Cu(acac)₂ dissolved in BE] was quickly injected into the mixture of OA, OAmine, HDD, and BE at the reflux temperature of BE (about 570 K), the solution turned red immediately. After 5 min, a dark-red colloid was collected. Figure 1e shows a typical TEM image of the as-prepared

Fig. 1 Characterization of the Cu nanoparticles in samples A, B, and C: **a** transmission electron microscopy (TEM) image and **b** selected-area electron diffraction (SAED) pattern for the Cu nanoparticles in sample A; **c** TEM image and **d** SAED pattern for the Cu nanoparticles in sample B; **e** TEM image and **f** high-resolution TEM (HRTEM) image of the Cu nanoparticles in sample C



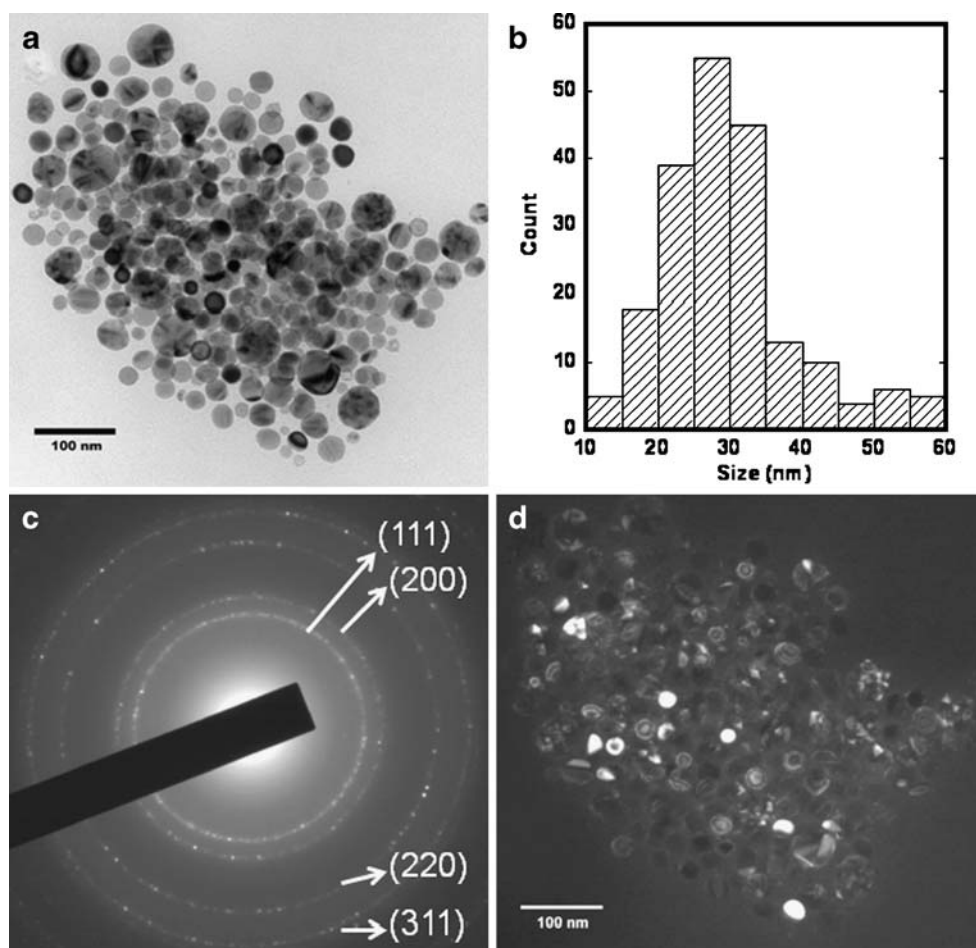
Cu nanoparticles in sample C. The average diameter was determined to be 70 nm with a standard deviation of 24 nm. Their SAED pattern is similar to the patterns for samples A and B (data not shown), indicating that the Cu nanoparticles in sample C adopt an fcc structure. Figure 1e shows a HRTEM image of part of a 70-nm Cu nanoparticle in sample C. The spacing of the lattice fringes in one direction is 0.20 nm, close to the d value of the Cu(111) plane.

Cu nanoparticles in sample D and their surface oxidation

The results show that large (more than 50 nm) fcc Cu nanoparticles can be obtained through thermal decomposition of Cu(ac) or thermal reduction of Cu(acac)₂. However, these

nanoparticles have a wide size distribution. To reduce both the size and the size distribution of as-prepared Cu nanoparticles, we used Cu(ac) as the precursor and HDD as the reducing agent and decreased the reaction temperature in the synthesis of sample D. The reaction was performed at 473 K, much lower than the decomposition temperature of Cu(ac). With the help of the reducing agent, the solution went through a similar color change during the increase of the reaction temperature as described for the synthesis of sample A: green, dark blue, green, yellow, dark brown, and burgundy. After 40 min at 473 K, a dark-red colloid was collected. Figure 2a shows a bright-field TEM image of the as-prepared Cu nanoparticles in sample D. It clearly shows that these Cu nanoparticles in sample D are much smaller than those in samples A, B, and

Fig. 2 Characterization of the Cu nanoparticles in sample D: **a** bright-field TEM image; **b** histogram of the particle size distribution; **c** SAED pattern; **d** dark-field TEM image for the same area as in **a**



C. Figure 2b shows the histogram of the size distribution obtained by measuring the diameters of 200 nanoparticles. The average diameter was determined to be 29 nm with a standard deviation of 9 nm. The smaller nanoparticles in Fig. 2a appear to have a homogeneous contrast within one nanoparticle. The larger nanoparticles clearly show the inhomogeneous contrast regions within one nanoparticle, indicating their polycrystalline structure. Figure 2c shows the SAED pattern of these nanoparticles, and four distinct diffraction rings are indexed as their corresponding fcc Cu crystalline planes. When TEM was performed in dark-field mode using a portion of the diffracted (111) beam, the same area as in Fig. 2a was examined and Fig. 2d shows its dark-field image. The bright spots in the dark-field image show the portions of the nanoparticles that have the (111) plane orientation. As can be seen, a few nanoparticles appear uniformly bright or dark for the whole area, indicating their single-crystalline structure. However, most of the bright spots in Fig. 1d are only part of the nanoparticles seen in Fig. 1a, in agreement with the polycrystalline structure of these nanoparticles. Therefore, the Cu nanoparticles in sample D are a mixture of single-crystalline and polycrystalline nanoparticles.

The HRTEM image of a 30-nm Cu nanoparticle in sample D in Fig. 3 reveals that only part of this nanoparticle

shows the lattice fringes. The spacing of these lattice fringes in this region is 0.20 nm, close to the d value of the Cu(111) plane. Also as indicated in the image, different lattice fringes can clearly be seen at the edge of the

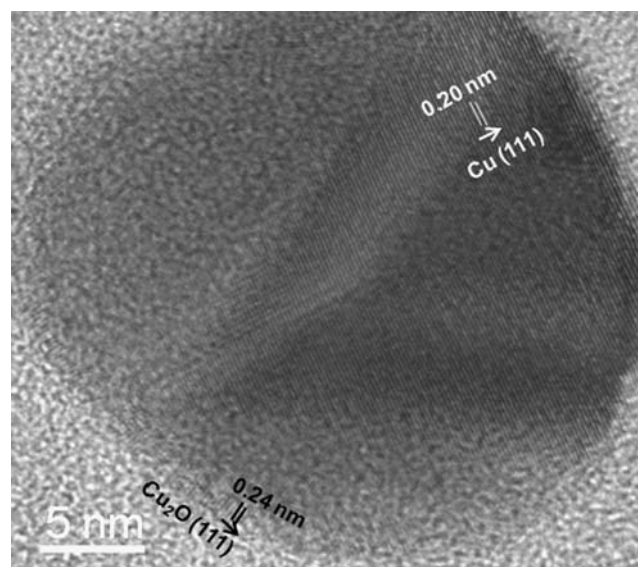


Fig. 3 HRTEM image of a Cu nanoparticle in sample D

nanoparticle. The spacing of these lattice fringes is 0.24 nm, close to the d value of the fcc Cu₂O (111) plane (cuprite, JCPDF no. 77-0199, $Pn-3m$, $a=0.4258$ nm, $d_{111}=0.24584$ nm, $d_{200}=0.21290$ nm, $d_{220}=0.15054$ nm, and $d_{311}=0.12838$ nm). None of the monoclinic CuO planes (tenorite, $C2/c$, JCPDF no. 65-2309) have this d value, indicating the surface of the as-prepared Cu nanoparticles is oxidized into fcc Cu₂O upon exposure to air. The thickness of this region is approximately 1 nm. However, the nanoparticle is not fully covered by a homogeneous Cu₂O layer, signifying a nonuniform surface oxidation.

Cu nanoparticles in sample E and their full oxidation

In comparison with the synthesis of sample D, we increased the amount of OA and OAmine in the synthesis of sample E, but the other synthetic conditions remained the same. The solution went through a similar color change during the increase of the reaction temperature as described for the synthesis of sample D. After 40 min at 473 K, a dark-red colloid was collected. However, unlike the colloids of samples A, B, C, and D, which remain dark red upon exposure to air, the extracted colloid of sample E immediately turned green upon exposure to air and remained green. Figure 4a shows a bright-field TEM image of the as-prepared Cu nanoparticles in sample E after their exposure to air. Compared with the Cu nanoparticles in Fig. 2a, these nanoparticles are smaller and monodisperse. Figure 4b shows the histogram of the size distribution obtained by measuring the diameters of 200 nanoparticles. The average diameter was determined to be 5.8 nm with a standard deviation of 0.8 nm. The corresponding values of the interplanar spacing for three distinct rings in the SAED pattern in Fig. 4c were calculated to be 0.25, 0.21, and 0.15 nm, which are different from the ones in Fig. 2c. These values match well with the ones for fcc Cu₂O. Therefore, the rings in Fig. 4c are indexed as their corresponding fcc Cu₂O crystalline planes. The HRTEM image for a 6-nm nanoparticle in Fig. 4d clearly shows that this nanoparticle is a single crystal. The spacing of the lattice fringes is 0.15 nm, close to the d value of the fcc Cu₂O (220) plane. In combination with the color change, we believe that these nanoparticles are fully oxidized upon exposure to air. Assuming that these Cu₂O nanoparticles are directly converted from Cu nanoparticles, after the density change from fcc Cu (8.02 g/cm³) [28] to fcc Cu₂O (6.0 g/cm³) [28] is taken into consideration, the size of pristine Cu nanoparticles is estimated to be 5.0 nm with a standard deviation of 0.7 nm.

CuS nanoplates from Cu nanoparticles in sample D

We have shown the reactivity of the Cu nanoparticles in samples D and E with respect to their oxidation upon

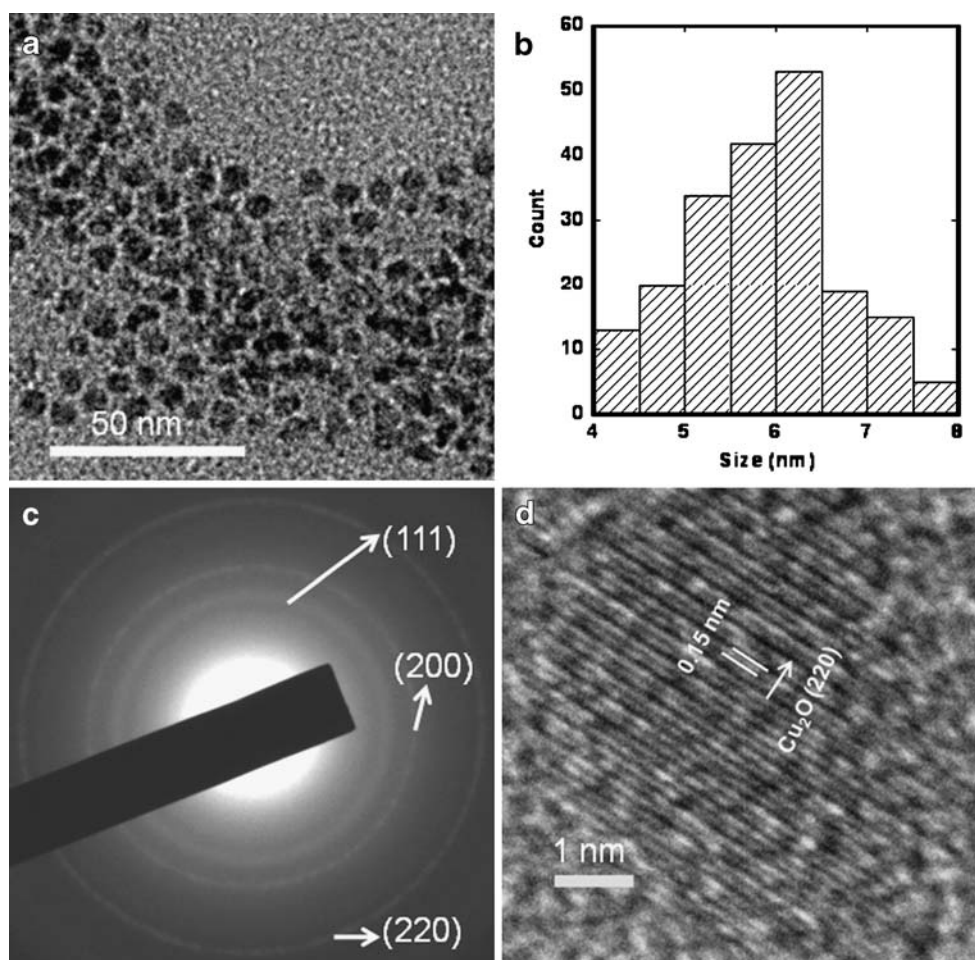
exposure to air. We have also utilized their reactivity and used these Cu nanoparticles as templates to synthesize more complex CuS nanostructures via the nanoscale Kirkendall effect. CuS adopts a unique hexagonal crystalline structure (covellite, JCPDF no. 78-0877, $P6_3/mmc$, $a=b=0.37938$ nm, $c=1.6341$ nm, $\alpha=\beta=90$, $\gamma=120$) with an axis ratio (a/c) of 1:4.3. Therefore, nanostructures different from spherical Cu nanoparticles are expected to be produced.

When the solution of S dissolved in BE was quickly injected into the colloid of sample D at 473 K under Ar, the dark-red colloid turned black immediately. After 20 min, a black colloid was collected. Figure 5a shows a typical TEM image of the as-prepared nanoparticles. These nanoparticles show morphologies different from those of the spherical Cu nanoparticles shown in Fig. 2a. Most of the nanoparticles exhibit hexagonal or quasi-hexagonal morphology (particles 1 and 2) and a few nanoparticles appear rod-like (particle 3). These morphologies are similar to the ones of the hexagonal CuS nanoplates reported in the literature [29–32] and suggest that the as-prepared nanoparticles are nanoplates. These nanoplates can be in either a face-down (particles 1 and 2) or a standing-up (particle 3) position. Among the nanoplates in a face-down position, approximately 80% are solid (particle 1) and the rest have a cavity around the center of the nanoplates (particle 2). Also, few aggregation-like nanoparticles are observed (particle 4); these are probably in an intermediate stage during the transformation from a spherical Cu nanoparticle to a CuS nanoplate.

Figure 5b shows the SAED pattern of these as-prepared nanoparticles. Seven distinct diffraction rings are observed and their corresponding interplanar spacing values were calculated to be 0.33, 0.31, 0.28, 0.23, 0.19, 0.17, and 0.16 nm. These values agree well with hexagonal CuS (JCPDF no. 78-0877, $d_{100}=0.32855$ nm, $d_{101}=0.32211$ nm, $d_{102}=0.30483$ nm, $d_{103}=0.28134$ nm, $d_{006}=0.27235$ nm, $d_{105}=0.23171$ nm, $d_{107}=0.19030$ nm, $d_{110}=0.18969$ nm, $d_{108}=0.17347$ nm, $d_{203}=0.15728$ nm, and $d_{116}=0.15566$ nm). Therefore, the rings in Fig. 5b are indexed as their corresponding hexagonal CuS crystalline planes. Figure 5c shows the histogram of the size distribution obtained by measuring the length of the longest diagonal of 200 face-down nanoplates. The average length was determined to be 52 nm with a standard deviation of 14 nm. The average thickness is 11 nm with a standard deviation of 3 nm.

Figure 6 shows the detailed HRTEM images of the four types of nanoparticles observed in Fig. 5a. Figure 6a shows the HRTEM image of a face-down solid hexagonal nanoplate and Fig. 6b shows the magnified HRTEM image in the selected area in Fig. 6a. Figure 6b clearly shows that this nanoplate is a single crystal. The spacing of the lattice

Fig. 4 Characterization of the Cu nanoparticles in sample E after exposure to air: **a** TEM image; **b** histogram of the particle size distribution; **c** SAED pattern; **d** HRTEM image



fringes is 0.32 nm, close to the d value of the hexagonal CuS (100) plane. The inset in Fig. 6b shows the fast Fourier transform (FFT) of the selected square area in Fig. 6b. In combination with the geometry of the hexagonal nanoplates, the FFT clearly shows that this face-down nanoplate is in the [001] beam direction (along the c axis) and is bound by six side planes: (100), (010), (-110), (-100), (0 -10), and (1 -10).

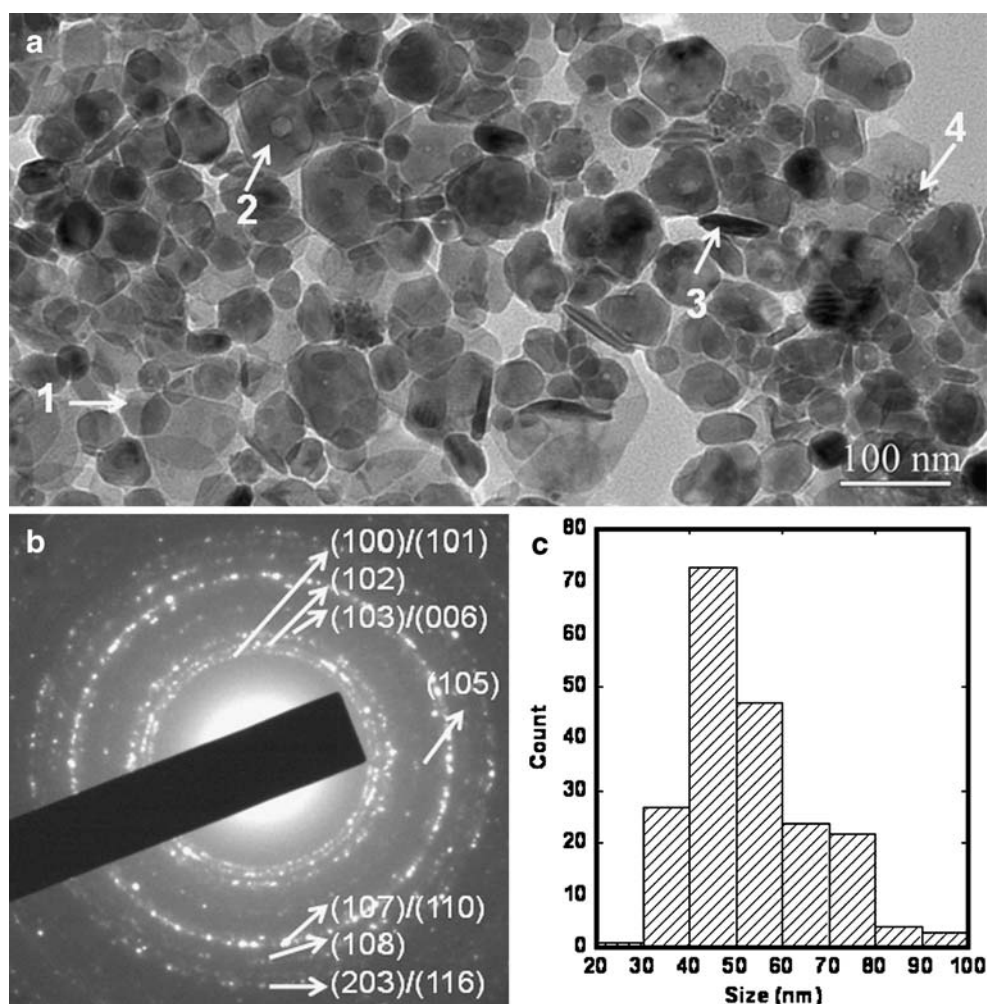
Figure 6c shows the HRTEM image of a face-down hexagonal nanoplate with a hexagonal cavity in the center and Fig. 6d shows its magnified HRTEM image in the selected area in Fig. 6c. Figure 6d shows that this nanoplate with a cavity in the center is also a single crystal. The lattice fringes can clearly be observed in the cavity region, indicating the hollow interior of this nanoplate. The spacing of the lattice fringes is 0.32 nm, close to the d value of the hexagonal CuS (100) plane. The inset in Fig. 6d shows the FFT of the selected square area in Fig. 6d. In combination with the geometry of the nanoplate and its cavity, the FFT clearly shows that this nanoplate and its cavity are in the [001] beam direction (along the c axis) and are bound by six side planes: (100), (010), (-110), (-100), (0 -10), and (1 -10).

Figure 6e shows the HRTEM image of a standing-up nanoplate. The spacing of the lattice fringes is 0.27 nm, close to the d value of the hexagonal CuS (006) plane and suggesting that this nanoplate is bound by two planes: (001) and (00 -1). Figure 6f shows the HRTEM image of an aggregation-like nanoplate, and the lattice fringes with different orientations within this nanoparticle indicate that this nanoparticle is probably on its way to forming a single-crystalline nanoplate.

CuS nanoplates from Cu nanoparticles in sample E

When the solution of S dissolved in BE was quickly injected into the colloid of sample E at 473 K under Ar, the dark-red colloid turned black immediately. After 20 min, a black colloid was collected. Figure 7a shows a TEM image of the as-prepared CuS nanoplates using Cu nanoparticles in sample E as the templates. Owing to their smaller size, the hexagonal shape for the face-down nanoplates is not as obvious as shown in Fig. 5a. However, as can be seen, the percentage of the standing-up nanoplates is much higher than in Fig. 5a. Also, for the face-down nanoplates, the contrast difference between the center region and edge

Fig. 5 Characterization of the CuS nanoplates produced from the Cu nanoparticles in sample D: **a** TEM image; **b** SAED pattern; **c** histogram of the particle length distribution



region indicates that these nanoplates are hollow. Figure 7b shows their SAED pattern. Five distinct diffraction rings are observed and their corresponding interplanar spacing values were calculated to be 0.33, 0.31, 0.28, 0.19, and 0.17 nm. These values agree well with hexagonal CuS and these rings are indexed as their corresponding hexagonal CuS crystalline planes. Figure 7c shows the histogram of the size distribution obtained by measuring the length of the longest diagonal of 200 face-down nanoplates. The average length was determined to be 12 nm with a standard deviation of 2 nm. Figure 7c shows the histogram of the size distribution obtained by measuring the thickness of 200 standing-up nanoplates. The average thickness is 5.1 nm with a standard deviation of 1.0 nm. Owing to their relatively narrow size distribution, the standing-up nanoplates also assemble into nanoribbons [30, 32] as shown in Fig. 7a.

Figure 8a shows the HRTEM image of a face-down hexagonal nanoplate. The spacing of the lattice fringes is 0.18 nm, close to the d value of the hexagonal CuS (110) plane. The inset in Fig. 8a shows the FFT of the selected square area in Fig. 8a. In combination with the geometry of

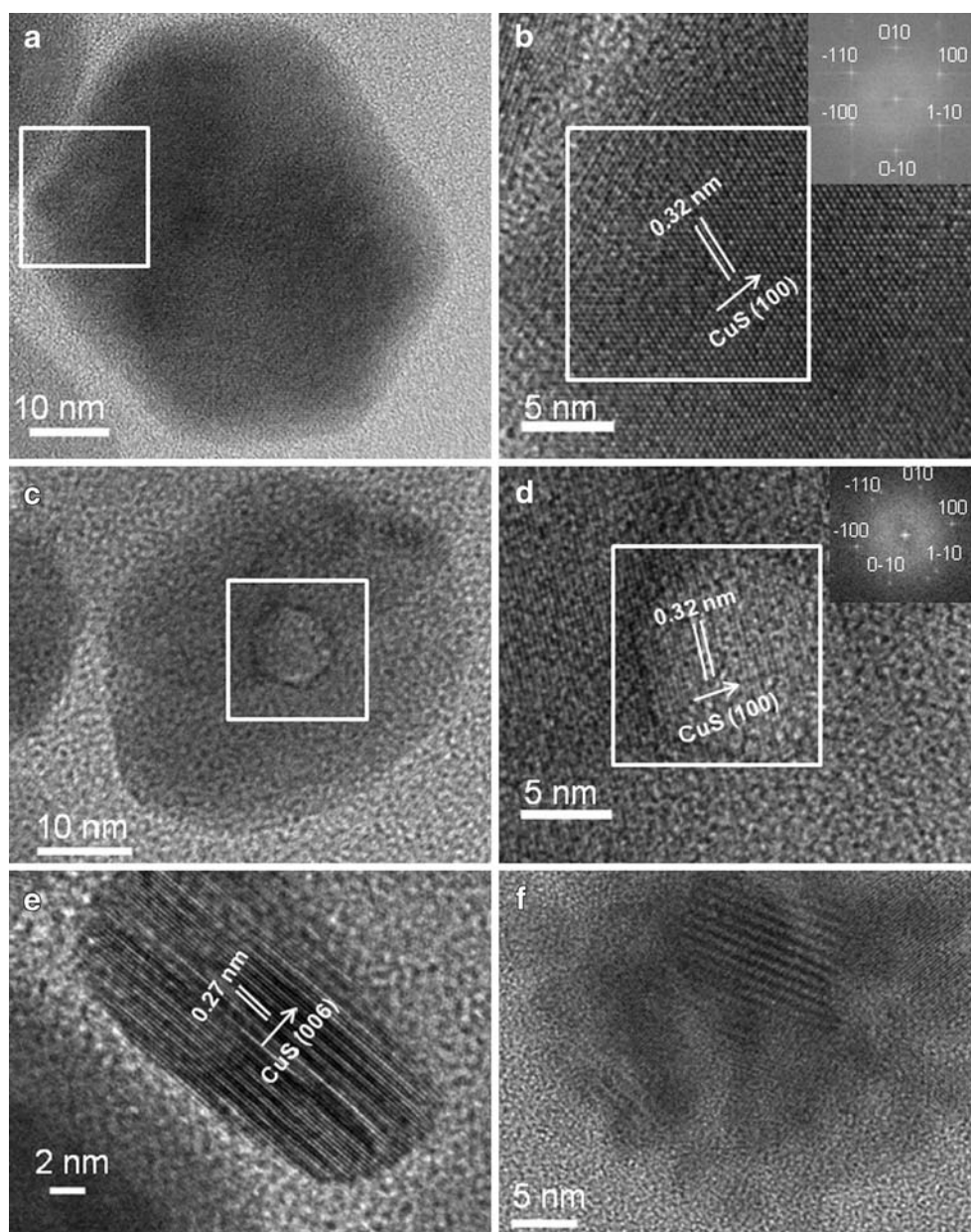
the hexagonal nanoplates, the FFT clearly shows that this face-down nanoplate is in the [001] beam direction (along the c axis) and is bound by six side planes: (110), (-120), (-210), ($1-10$), ($1-20$), and ($2-10$). Figure 8b shows the HRTEM image of two standing-up nanoplates. The spacing of their lattice fringes is 0.27 nm, close to the d value of the hexagonal CuS (006) plane and suggesting that both of these nanoplates are bound by two planes: (001) and (00-1).

Discussion

Synthesis of Cu nanoparticles

As shown in Fig. 1a, during the synthesis of sample A using the thermal decomposition of Cu(ac) at 523 K, Cu nanorods are also obtained. Cu nanorods produced as by-products during the synthesis of spherical Cu nanoparticles have been demonstrated in the literature [11–13, 16]. For example, Cu nanorods and spherical Cu nanoparticles have been synthesized in one pot via the reduction of copper(II) bis(2-ethylhexyl)sulfosuccinate using hydrazine [11–13].

Fig. 6 HRTEM images of the CuS nanoplates produced from the Cu nanoparticles in sample D. **a** A face-down solid hexagonal nanoplate. **b** Magnified HRTEM image in the selected area in **a**. The *inset* shows the fast Fourier transform (FFT) for the selected area in **b**. **c** A face-down hexagonal nanoplate with a hexagonal cavity. **d** Magnified HRTEM image of the selected area in **c**. The inset shows the FFT for the selected area in **d**. **e** A standing-up nanoplate. **f** A nanoplate being formed

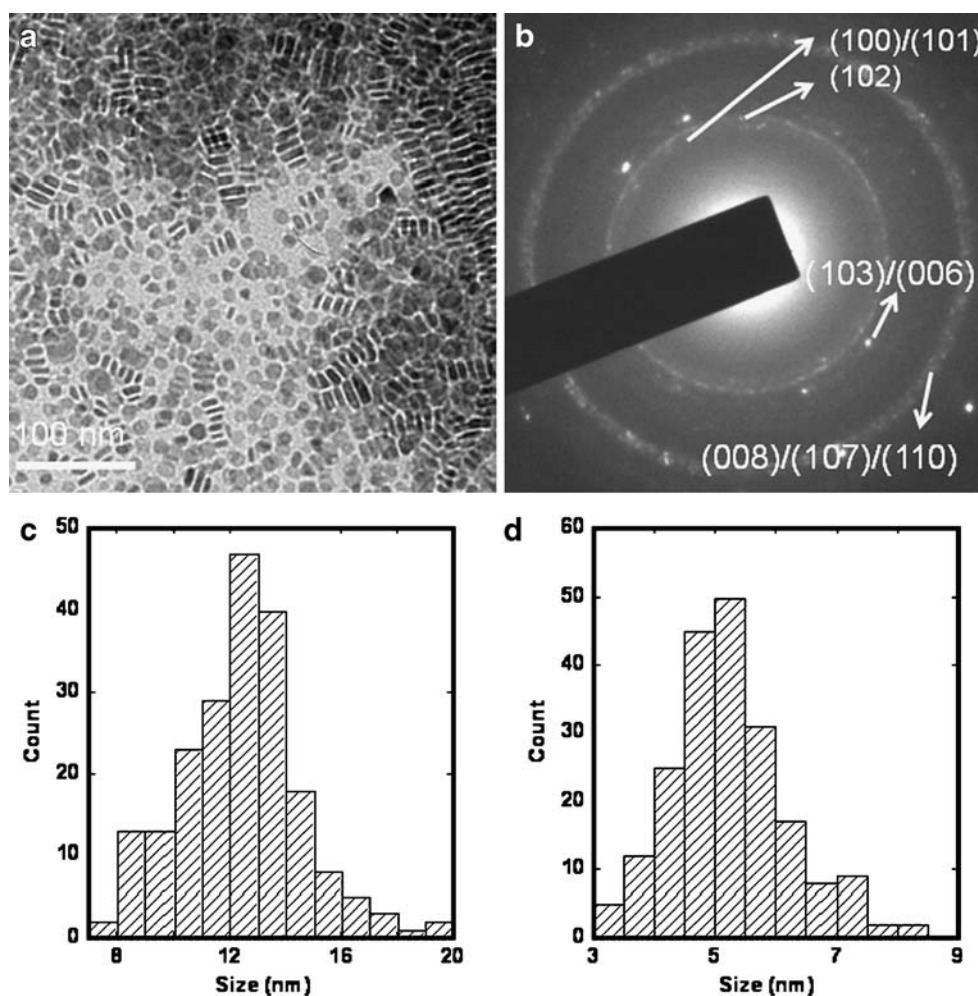


The interconnected cylindrical reverse micelles used as templates in the synthesis were believed to play an important role in the formation of these nanorods [11]. Another study on the synthesis of Cu nanoparticles via the thermal reduction of $\text{Cu}(\text{acac})_2$ using HDD in octyl ether showed the formation of Cu nanorods and nanocubes along with spherical Cu nanoparticles when the reaction temperature was above 463 K [16]. The surfactants, OA and OAm, were proposed to regulate the growth of these nanorods from the decahedral seeds [16]. However, in our syntheses of samples B and C, no Cu nanorods were obtained at 570 K. Large (more than 50 nm) decahedral Cu nanoparticles are observed frequently.

Both the template model and the surfactant regulation model are insufficient to explain some of the typical

phenomena observed in the synthesis of colloidal nanoparticles [33]. For example, nanoparticles with multiple shapes can be formed in one pot during a single homogeneous reaction. A kinetics-based mechanism was proposed to explain the appearance of both isotropic and anisotropic nanoparticles for fcc Au and Ag nanoparticles [33]. The strain in decahedral seeds can cause the elongation of decahedra by growing the side faces, resulting in the formation of nanorods and nanowires. This model can explain the appearance of both spherical Cu nanoparticles and Cu nanorods in our synthesis of sample A. The disappearance of Cu nanorods and the frequent appearance of the large decahedral nanoparticles in the syntheses of samples B and C indicate that, under these synthetic conditions, instead of growing the side faces, the

Fig. 7 Characterization of the CuS nanoplates produced from the Cu nanoparticles in sample E: **a** TEM image; **b** SAED pattern; **c** histogram of the nanoplate length distribution; **d** histogram of the nanoplate thickness distribution



decahedral seeds grow and enlarge themselves laterally by introducing the defects to release the strain [34, 35].

In the synthesis of Co and Ni nanoparticles, the rapid injection of the precursor solution yields a highly supersaturated solution, resulting in a fast nucleation and a narrow size distribution [17–22]. However, this is not the case in the synthesis of sample C. In comparison with the synthesis of sample B, the quick injection of the Cu precursor solution at the reflux temperature of BE does not significantly change the morphologies of as-prepared Cu nanoparticles in terms of their wide size distribution. We also increased the amount of OA and OAmes fivefold for this quick injection reaction to control the size of as-prepared nanoparticles. However, there is no significant change in morphology from that of sample C. This evidence suggests the growth of Cu nanoparticles at 570 K is very fast. It is hard to control their size and size distribution by simply changing the amount of surfactants used in the synthesis.

When $\text{Cu}(\text{acac})_2$ was replaced with $\text{Cu}(\text{ac})$ as the Cu precursor and the reaction was performed at 473 K in the synthesis of sample D, the average size of the Cu nanoparticles was reduced to 29 nm. As we increased the amount

of OA and OAmes in the synthesis of sample E, the average size and size distribution of the Cu nanoparticles were greatly reduced, suggesting that the surfactants play an important role in the growth of Cu nanoparticles under these synthetic conditions. As a result, controlling the size and size distribution of the as-prepared nanoparticles can be achieved by tuning the amount of the surfactants used in the synthesis.

Oxidization of Cu nanoparticles

In our previous work, we investigated the effect of size on the oxidation of Co nanoparticles using extended X-ray absorption fine structure and X-ray absorption near-edge structure and showed that the smaller the nanoparticles are, the more reactive they are with respect to oxidization in air [17]. Recently, we also demonstrated the formation of a nonuniform cobalt oxide layer at the surface of colloidal Co nanoparticles during their natural aging in air using HRTEM [21]. In the case of Cu nanoparticles, our results clearly show a similar oxidization behavior and size effect.

The HRTEM image of a Cu nanoparticle (30 nm) in sample D after its exposure to air in Fig. 3 shows that the

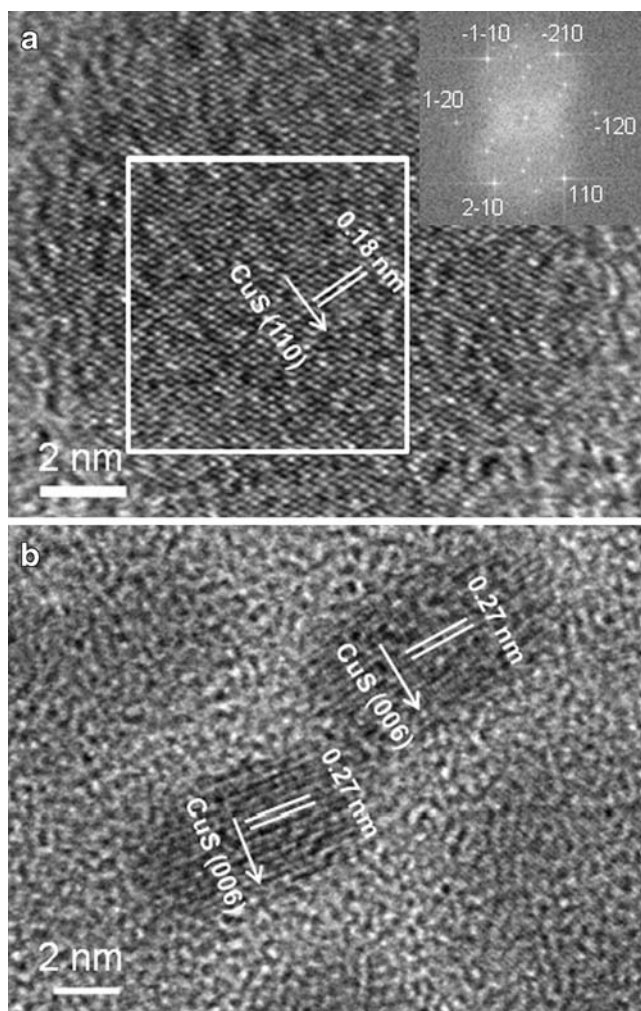


Fig. 8 HRTEM images of the CuS nanoplates produced from the Cu nanoparticles in sample E. **a** A face-down nanoplate. The inset shows the FFT of the selected area in **a**. **b** Standing-up nanoplates

surface of the freshly prepared Cu nanoparticles can be oxidized to Cu_2O quickly, though the Cu_2O layer is not homogeneous. The colloid of sample D remains dark red for at least 3 months, indicating that the full oxidization of nanoparticles takes much longer. The immediate color change of the colloid of sample E upon exposure to air suggests that these Cu nanoparticles in sample E are much more reactive than those in sample D with respect to oxidization in air. The HRTEM result confirms the full conversion of Cu nanoparticles into Cu_2O nanoparticles.

In bulk, Cu_2O is not stable and can be easily oxidized into CuO in air at room temperature. Studies of the effect of size on the crystal structures of copper oxides have shown that the cubic Cu_2O is more stable than the monoclinic CuO below 25 nm since high-symmetry crystal structures are more likely to be stable at smaller sizes [36]. It has also been reported that stable colloidal Cu_2O nanoparticles can be produced simply by redispersing purified freshly

prepared colloidal Cu nanoparticles in hexane [15]. The Cu nanoparticles in hexane are gradually oxidized to Cu_2O nanoparticles. The high-symmetry cubic structure shared by Cu and Cu_2O was believed to be the driving force in this transformation [15]. A crystalline reconstruction is needed for the transformation from fcc Cu to monoclinic CuO. Our results on the surface oxidization of the Cu nanoparticles in sample D and the full oxidization of the Cu nanoparticles in sample E are in good agreement with these results and show that stable Cu_2O nanoparticles can be prepared.

Sulfidation of Cu nanoparticles

Along with the natural oxidization of Cu nanoparticles, sulfidation provides us with another way to chemically transform these Cu nanoparticles as demonstrated in the synthesis of CuS nanoplates. The effect of size on this reaction is manifested in the different sizes of the CuS nanoplates produced from samples D and E. The average length and thickness of the CuS nanoplates from the Cu nanoparticles in sample D with average size of 29 nm are 52 and 11 nm, whereas their counterparts from the Cu nanoparticles in sample E with average size of 5 nm are 12 and 5 nm. A rough estimation based on these values indicates that not all of the CuS nanoplates can be solid and, if not all of them are solid, some of them must have cavities, which are commonly found in the nanostructures prepared through the nanoscale Kirkendall effect [4–7].

When the Cu nanoparticles in sample D were used to synthesize CuS, both solid CuS nanoplates and CuS nanoplates with different cavity sizes were observed (Figs. 5 and 6). Recent studies have demonstrated that hollow silver (I) selenide nanoparticles are obtained when single-crystalline Ag nanoparticles are used as templates in the synthesis through the nanoscale Kirkendall effect, whereas solid single-crystalline silver(I) selenide nanoparticles are produced when multiply twinned Ag nanoparticles are used [37]. The defects in the multiply twinned nanoparticles are believed to create other reaction paths to suppress the formation of a cavity during the reaction [37]. In our experiments, the Cu nanoparticles in sample D are a mixture of single-crystalline and polycrystalline Cu nanoparticles. Therefore, the CuS nanoplates with cavities are probably converted from the single-crystalline Cu nanoparticles, whereas the solid CuS nanoplates are from the polycrystalline Cu nanoparticles. On the basis of the single-crystalline Cu_2O nanoparticles produced from the Cu nanoparticles in sample E upon exposure to air, these pristine Cu nanoparticles are likely single crystals. Therefore, the CuS nanoplates produced from the Cu nanoparticles in sample E are hollow. Figure 7a clearly shows the contrast between the center and edge regions in these face-down CuS nanoplates.

The different morphologies of the Cu₂O nanoparticles produced through oxidization and the CuS nanoplates produced through sulfidation of Cu nanoparticles reflect the different diffusion behaviors involved in these two transformations. The formation of the solid Cu₂O nanoparticles from the Cu nanoparticles in sample E upon exposure to air indicates that this oxidization involves the direct diffusion of O₂ into the fcc Cu crystalline structure, which is also shown in the surface oxidization of the Cu nanoparticles in sample D, whereas the formation of the hollow CuS nanoplates from the Cu nanoparticles in sample E during sulfidation suggests the Cu outward diffusion is faster than S inward diffusion. Two factors are believed to contribute to these two different diffusion behaviors. One is the different reaction temperatures (sulfidation was performed at a much higher temperature than oxidization), and the other is the different crystalline structures of fcc Cu₂O and hexagonal CuS. The transformation from Cu nanoparticles to Cu₂O nanoparticles only involves the diffusion of O₂ into the Cu structure. During the sulfidation, both Cu outward diffusion and S inward diffusion are involved and a reconstruction of the fcc Cu structure is required to form CuS nanoplates. Since the isotropic Cu nanoparticles are used as templates, Cu outward diffusion and S inward diffusion can be in all directions. The formation of CuS nanoplates suggests that the intrinsic hexagonal CuS structure is another critical factor in this transformation and the growth rate along the *c* axis is much slower than that along the hexagonal *a*–*b* plane.

Conclusion

Colloidal Cu nanoparticles with an fcc structure were synthesized in the presence of surfactants in an organic solvent under an Ar environment. Large (more than 50 nm) Cu nanoparticles can be obtained through thermal decomposition of Cu(ac) or thermal reduction of Cu(acac)₂ using HDD at 570 K. Through the thermal reduction of Cu(ac) using HDD at 473 K, the average size of the Cu nanoparticles can be tuned from 29 to 5 nm by increasing the amount of the surfactants used in the synthesis. TEM, SAED, and HRTEM were used to characterize these Cu nanoparticles and their chemical reactivity with respect to the oxidization and sulfidation. The effect of size is manifested in these two chemical transformations. Whereas the surfaces of Cu nanoparticles with an average diameter of 29 nm can be oxidized into fcc Cu₂O upon exposure to air, Cu nanoparticles with an average diameter of 5 nm are immediately and fully oxidized into stable fcc Cu₂O nanoparticles. This full oxidization involves the direct diffusion of O₂ into the fcc Cu crystalline structure. When monodisperse 5-nm Cu nanoparticles are used during sulfidation, hollow CuS nano-

plates are formed and standing-up nanoplates assemble into nanoribbons. When a mixture of single-crystalline and polycrystalline Cu nanoparticles with an average diameter of 29 nm is used as the template during sulfidation, solid and hollow hexagonal CuS nanoplates are produced. The formation of hollow CuS nanoplates suggests the Cu outward diffusion and the S inward diffusion are involved during sulfidation. Cu outward diffusion is faster than S inward diffusion. The formation of solid CuS nanoplates is likely attributed to the defects in the polycrystalline Cu nanoparticles. The different reaction temperatures and intrinsic crystalline structures of Cu₂O and CuS contribute to the different diffusion and growth behaviors for oxidization and sulfidation. Our work clearly shows that size plays an important role in the reactivity of Cu nanoparticles, and their chemical reactivity can be utilized to synthesize stable Cu₂O and CuS nanoparticles. The sulfidation of Cu nanoparticles can be readily extended to the synthesis of the whole family of copper sulfides.

Acknowledgements We thank Li-Chung Lai and Wen-An Chiou for their help with TEM measurements. We acknowledge the support of the Maryland NanoCenter and its NispLab. The NispLab is supported in part by the NSF as an MRSEC Shared Experimental Facility.

References

1. Yin Y, Alivisatos AP (2005) *Nature* 437:664–670
2. Tao AR, Habas S, Yang PD (2008) *Small* 4:310–325
3. Xia Y, Xiong YJ, Lim B, Skrabalak SE (2009) *Angew Chem Int Ed* 48:60–103
4. Yin YD, Rioux RM, Erdonmez CK, Hughes S, Somorjai GA, Alivisatos AP (2004) *Science* 304:711–714
5. Yin YD, Erdonmez CK, Cabot A, Hughes S, Alivisatos AP (2006) *Adv Funct Mater* 16:1389–1399
6. Cabot A, Puentes VF, Shevchenko E, Yin Y, Balcells L, Marcus MA, Hughes SM, Alivisatos AP (2007) *J Am Chem Soc* 129:10358–10360
7. Cabot A, Smith RK, Yin YD, Zheng HM, Reinhard BM, Liu HT, Alivisatos AP (2008) *ACS Nano* 2:1452–1458
8. Lewinski N, Colvin V, Drezek R (2008) *Small* 4:26–49
9. Grassian VH (2008) *J Phys Chem C* 112:18303–18313
10. Lisiecki I, Pileni MP (1993) *J Am Chem Soc* 115:3887–3896
11. Tanori J, Pileni MP (1997) *Langmuir* 13:639–646
12. Salzemann C, Lisiecki I, Brioude A, Urban J, Pileni MP (2004) *J Phys Chem B* 108:13242–13248
13. Salzemann C, Lisiecki L, Urban J, Pileni MP (2004) *Langmuir* 20:11772–11777
14. Murray CB, Kagan CR, Bawendi MG (2000) *Annu Rev Mater Sci* 30:545–610
15. Yin M, Wu CK, Lou YB, Burda C, Koberstein JT, Zhu YM, O'Brien S (2005) *J Am Chem Soc* 127:9506–9511
16. Mott D, Galkowski J, Wang LY, Luo J, Zhong CJ (2007) *Langmuir* 23:5740–5745
17. Cheng GJ, Carter JD, Guo T (2004) *Chem Phys Lett* 400:122–127
18. Cheng GJ, Romero D, Fraser GT, Walker ARH (2005) *Langmuir* 21:12055–12059
19. Cheng GJ, Dennis CL, Shull RD, Walker ARH (2007) *Langmuir* 23:11740–11746

20. Cheng GJ, Shull RD, Walker ARH (2009) *J Magn Magn Mater* 321:1351–1355
21. Cheng GJ, Dennis CL, Shull RD, Walker ARH (2009) *Cryst Growth Des* 9:3714–3720
22. Cheng GJ, Puentes VF, Guo T (2006) *J Colloid Interface Sci* 293:430–436
23. Bruneval F, Vast N, Reining L, Izquierdo M, Sirotti F, Barrett N (2006) *Phys Rev Lett* 97:267601
24. Gou LF, Murphy CJ (2003) *Nano Lett* 3:231–234
25. Zhao YX, Pan HC, Lou YB, Qiu XF, Zhu JJ, Burda C (2009) *J Am Chem Soc* 131:4253–4261
26. Wang ZL (2000) *J Phys Chem B* 104:1153–1175
27. Ding Y, Wang ZL (2004) *J Phys Chem B* 108:12280–12291
28. Lide DR (ed) (2008) *CRC handbook of chemistry and physics*, 88th edn. CRC, Boca Raton
29. Wang KJ, Li GD, Li JX, Wang Q, Chen JS (2007) *Cryst Growth Des* 7:2265–2267
30. Ghezelbash A, Korgel BA (2005) *Langmuir* 21:9451–9456
31. Goncalves AP, Lopes EB, Casaca A, Dias M, Almeida M (2008) *J Cryst Growth* 310:2742–2745
32. Li BX, Xie Y, Xue Y (2007) *J Phys Chem C* 111:12181–12187
33. Lofton C, Sigmund W (2005) *Adv Funct Mater* 15:1197–1208
34. Ascencio JA, Gutierrez-Wing C, Espinosa ME, Marin M, Tehuacanero S, Zorrilla C, Jose-Yacaman M (1998) *Surf Sci* 396:349–368
35. Hofmeister H (1998) *Cryst Res Technol* 33:3–25
36. Palkar VR, Ayyub P, Chattopadhyay S, Multani M (1996) *Phys Rev B* 53:2167–2170
37. Tang Y, Ouyang M (2007) *Nat Mater* 6:754–759